



Article

Dynamic Monitoring of Surface Water Bodies and Their Influencing Factors in the Yellow River Basin

Zikun Zhao ¹, Huanwei Li ¹, Xiaoyan Song ^{2,*} and Wenyi Sun ³

¹ College of Water Resource and Architectural Engineering, Northwest A&F University, Xianyang 712100, China; 893225748@nwafu.edu.cn (Z.Z.); lihuanwei@nwafu.edu.cn (H.L.)

² Key Laboratory of Agricultural Soil and Water Engineering in Arid and Semi-Arid Areas, Ministry of Education, Northwest A&F University, Xianyang 712100, China

³ State Key Laboratory of Soil Erosion and Dryland Farming on the Loess Plateau, Institute of Soil and Water Conservation, Northwest A&F University, Xianyang 712100, China; sunwy@ms.iswc.ac.cn

* Correspondence: xiaoyansong@nwsuaf.edu.cn; Tel.: +86-13759949150

Abstract: Surface water bodies exhibit dynamic characteristics, undergoing variations in size, shape, and flow patterns over time due to numerous natural and human factors. The monitoring of spatial-temporal changes in surface water bodies is crucial for the sustainable development and efficient utilization of water resources. In this study, Landsat series images on the Google Earth Engine (GEE) platform, along with the HydroLAKES and China Reservoir datasets, were utilized to establish an extraction process for surface water bodies from 1986 to 2021 in the Yellow River Basin (YRB). The study aims to investigate the dynamics of surface water bodies and the driving factors within the YRB. The findings reveal an overall expansion tendency of surface water bodies in the YRB between 1986 and 2021. In the YRB, the total area of surface water bodies, natural lakes, and artificial reservoirs increased by 2983.8 km² (40.4%), 281.1 km² (11.5%), and 1017.6 km² (101.7%), respectively. A total of 102 natural lakes expanded, while 23 shrank. Regarding artificial reservoirs, 204 expanded, and 77 shrank. The factors that contributed most to the increase in the surface water bodies were increasing precipitation and reservoir construction, whose contribution rates could reach 47% and 32.6%, respectively. Additionally, the rising temperatures melted permafrost, ice, and snow, positively correlating with water expansion in the upper reaches of the YRB, particularly natural lakes.



Citation: Zhao, Z.; Li, H.; Song, X.; Sun, W. Dynamic Monitoring of Surface Water Bodies and Their Influencing Factors in the Yellow River Basin. *Remote Sens.* **2023**, *15*, 5157. <https://doi.org/10.3390/rs15215157>

Academic Editor: Frédéric Frappart

Received: 18 September 2023

Revised: 22 October 2023

Accepted: 26 October 2023

Published: 28 October 2023



Copyright: © 2023 by the authors. Licensee MDPI, Basel, Switzerland. This article is an open access article distributed under the terms and conditions of the Creative Commons Attribution (CC BY) license (<https://creativecommons.org/licenses/by/4.0/>).

Keywords: surface water bodies; natural lakes; artificial reservoirs; the Yellow River Basin; GEE platform

1. Introduction

Surface water bodies, including lakes, rivers, reservoirs (artificial lakes), ponds, and ditches, are the basis for human survival and have a significant impact on regional economic and social development. Surface water bodies make up only around 0.8% of the land surface but provide domestic water for nearly 78% of urban residents [1]. Natural lakes and rivers represent the majority, accounting for approximately 88% of the surface water bodies accessible for human utilization, serving as the primary source of surface water resources [2]. Beyond supplying basic water for human survival, surface water resources play a key role in industrial production and agricultural irrigation within human society [3,4]. Recently, there has been a significant shift in the state of water resources and the pattern of the water cycle, primarily driven by climate changes and intensified human activities [5]. Therefore, monitoring the spatio-temporal dynamics of surface water bodies is crucial for promoting the rational utilization of water resources, protecting the ecological environment, and fostering the sustainable development of both society and economy.

The development of remote sensing technology provides a valuable database for resource surveys, environmental assessment, and disaster monitoring across various temporal and spatial scales. Remote sensing, with its advantages of real-time performance,

wide coverage, and rapid data updates, has emerged as an important technology for monitoring water bodies' dynamics. Previous studies have explored the dynamics of surface water at different scales, ranging from regional to global, using optical sensors such as MODIS [6–8], Landsat [9–12], and Sentinel [13,14]. The extraction of water bodies is mainly automatic methods involving support vector machines [15,16], decision trees [17], object-oriented methods [18], and so on. These methods are target-based image classification whose accuracy is limited by the training sample selection [19]. The pixel-based thresholding method, which identifies water bodies based on the threshold of water indices, is favored due to its relatively simple operation and high accuracy. The widely utilized water indices include the Normalized Difference Water Index (NDWI) [20], the Modified Normalized Difference Water Index (MNDWI) [21], and the Automated Water Extraction Index (AWEI) [11]. However, since the spectral signature of the same ground objects varies in different external environments, it is challenging to distinguish water bodies using a single ideal threshold [22]. The Otsu algorithm solves this problem by automatically determining the optimal threshold [23,24], but this algorithm is difficult to ensure the accuracy of local water extraction in large watersheds [25]. The synthesis and optimization of multiple indicators are important for improving the extraction accuracy of surface water bodies.

Surface water bodies are affected by seasonal rainfall and are dynamic systems that rely on high spatial-temporal resolution satellite remote sensing imagery, requiring the processing of a large volume of these images. Traditional image processing methods have a low level of automation, long time consuming, and intensive labor, making it challenging for long-term dynamic monitoring of surface water bodies. The emergence of cloud computing platforms has significantly improved the processing of geospatial data, allowing for large-scale analysis without requiring extensive expertise and effort. Among these platforms, Google Earth Engine (GEE), as an archetypal cloud-based platform, exhibits expedited data processing capabilities, operating intrinsically and in parallel, ensuring optimal performance. GEE boasts extensive repositories housing multi-petabytes of remote sensing data, greatly enhancing the efficiency of image processing [26,27]. The GEE platform has been successfully applied in various fields, such as the mapping of forests [28], urban land [29], coastal tidal flats [30], as well as surface water bodies [31–33]. For example, Pekel, Cottam, Gorelick, and Belward [31] completed mapping of worldwide surface water bodies spanning the time period from 1984 to 2015 based on GEE, and Zou et al. [32] also explored the connectivity of surface water bodies in the United States, over the temporal span from 1984 to 2016.

The shortage of water resources in the Yellow River Basin (YRB) is prominent, and it will continue to be a challenge in the future due to climate change and increased human activities. With only 2% of the nation's river runoff, the YRB supplies water for over 12% of the Chinese population and irrigates more than 15% of China's farmland [34]. Due to global warming and the implementation of the "Grain to Green" Project, the reduction in runoff observed in YRB since the late 1980s was an unprecedented event within the historical record over the past 500 years [35]. There is a lack of systematic research on how the surface water body area of the YRB has changed. Şerban et al. [36] explored the thermokarst lakes and ponds situated within the source regions of the YRB, employing the supervised Maximum Likelihood Classification method with Landsat imagery for three periods: 1986, 2000, and 2015. Zhou et al. [37] revealed the changes in surface water bodies area in the source regions of the YRB from 1986 to 2019 using the GEE. Some other studies focus on long-term changes in local areas of the YRB, such as the Hetao Plain and the Xiaolangdi Reservoir [38,39]. There is a lack of comprehensive studies that examine the long-term changes in surface water bodies for the entire YRB, and more detailed spatial descriptions of the impacts of climate change and reservoir construction on surface water bodies changes in the YRB are still lacking.

The main purposes of this study are (1) to construct the extraction process of surface water bodies during 1986–2021 in the YRB using Landsat series images on the GEE platform, (2) to reveal the temporal and spatial dynamics of surface water bodies within distinct

sub-regions, as well as their natural lakes and artificial reservoirs, and (3) to attribute the influences of climate fluctuations and anthropogenic activities on changes in surface water bodies. This study can enhance the comprehension of climate-driven and human-influenced surface water bodies and provide important insight for policymakers to formulate effective and sustainable water resource management policies.

2. Materials and Methods

2.1. Study Areas

The Yellow River, located in northern China, is the country's second-largest river, with a total length of approximately 5464 km. It covers an area of nearly 795,000 km² (8.3% of China's area) and has a variety of topographical and climate features. Based on the flow direction, the YRB experiences three typical landforms: the Qinghai-Tibet Plateau, boasting an average elevation surpassing 3500 m; the Loess Plateau, with an average elevation of 2000 m, and an alluvial plain [40]. The YRB experiences a continental monsoon climate, displaying arid, semi-arid, and semi-humid characteristics. Precipitation levels increase from northwest to southeast, with the annual mean precipitation ranging from 368 to 670 mm. The average annual temperature in the region ranges from 4 to 14 °C [41].

To consider the regional differences of surface water bodies in the YRB, the eight sub-basins are divided according to the secondary basin boundary (Figure 1). The eight sub-basins along the flow direction of the Yellow River are upper of Longyang Gorge (ULG), Longyang Gorge to Lanzhou (LTL), Lanzhou to Hekou (LTH), the interior drainage area (IDA), Hekou to Longmen (HTL), Longmen to Sanmenxia (LTS), Sanmenxia to Huayuankou (STH), and the lower of Huayuankou (LOH).

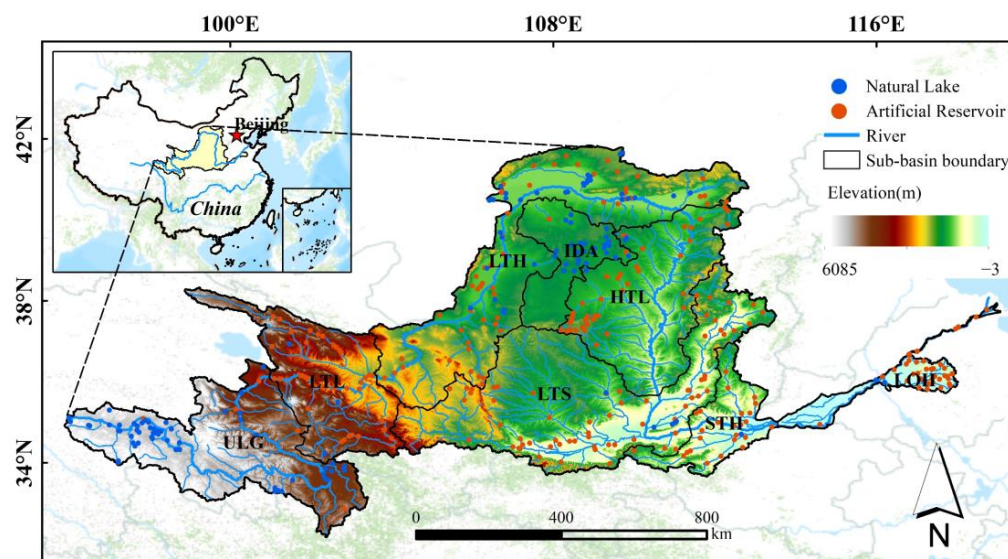


Figure 1. The location and geographical features of the Yellow River Basin.

2.2. Data Sources

Nearly all Landsat 5/7/8 surface reflectance images, totaling 64,620 scenes with cloud cover less than 30%, were utilized (Figure 1). The Landsat images used in this study ensured both a sufficient number of images and a lower cloud cover. These images were atmospherically corrected using the LEDAPS algorithm and were acquired from the GEE platform (<https://earthengine.google.com/>, accessed on 1 January 2022). The entire study area covers 72 Landsat paths/rows of the Worldwide Reference System (WRS-2), and the spatial distribution of good-quality observations is shown in Figure 2a. The number of images acquired annually varies from 382 in 1986 to 2623 in 2021 (Figure 2b).

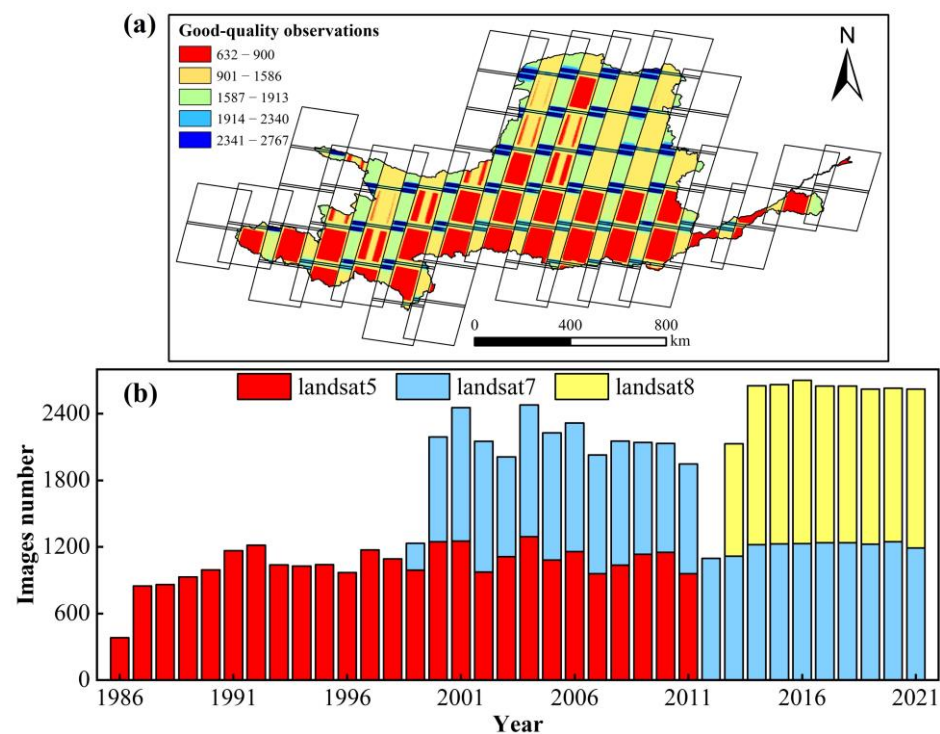


Figure 2. Distribution and numbers of Landsat images in the YRB in 1986–2021. (a) Distribution of good-quality images of Landsat series images, and (b) annual variation in the number of Landsat images.

The NASA Digital Elevation Model (NASADEM) is utilized as auxiliary data to generate a slope mask, which aids in the removal of terrain shadow pixels that might be mistakenly classified as water pixels. The HydroLAKES dataset (<https://www.hydrosheds.org/>, accessed on 1 January 2022) and China Reservoir Dataset (CRD) [42] are employed to generate lake masks and reservoir masks, respectively. In order to evaluate the accuracy of the water information extracted in this study, Sentinel-2 images are utilized to derive the water and non-water samples. The results obtained in the study are also compared with the Joint Research Centre Global Surface Water Dataset (JRC-data) [31].

Precipitation, air temperature, and water surface evaporation are selected as representations of climatic factors, ignoring negligible factors (i.e., sunshine duration and humidity) [17,43]. These datasets are collected from ERA5 reanalysis hourly data (<https://www.ecmwf.int/>, accessed on 1 January 2022), which have been validated for reliability with station observations [44,45].

2.3. Methods

2.3.1. Water Extraction Algorithm

The MNDWI has been widely utilized for surface water extraction [46], and it was an extension of NDWI. However, MNDWI is subject to commission errors in pixels, especially when the pixels comprise surface water bodies and vegetation cover [47]. Combining MNDWI, Enhanced Vegetation Index (EVI), and Normalized Vegetation Index (NDVI) is more stable and effective than individual indices in extracting surface water bodies [48]. Therefore, a combination of MNDWI, EVI, and NDVI is used to detect surface water bodies in this study. The criteria employed ($MNDWI > EVI$ or $MNDWI > NDVI$) have been proven to be effective in water information extracting based on water signals and are stronger than vegetation signals. Moreover, the criteria of $EVI < 0.1$ can reduce the interference from

wetland vegetation. Therefore, this study extracts surface water bodies utilizing the criteria of ((MNDWI > EVI or MNDWI > NDVI) and (EVI < 0.1)).

$$\text{MNDWI} = \frac{\rho_{\text{Green}} - \rho_{\text{SWIR}}}{\rho_{\text{Green}} + \rho_{\text{SWIR}}} \quad (1)$$

$$\text{EVI} = 2.5 \times \frac{\rho_{\text{NIR}} - \rho_{\text{Red}}}{\rho_{\text{NIR}} + 6 \times \rho_{\text{Red}} - 7.5 \times \rho_{\text{Blue}} + 1} \quad (2)$$

$$\text{NDVI} = \frac{\rho_{\text{NIR}} - \rho_{\text{Red}}}{\rho_{\text{NIR}} + \rho_{\text{Red}}} \quad (3)$$

where ρ_{NIR} , ρ_{Red} , ρ_{Blue} , ρ_{Green} and ρ_{SWIR} are near-infrared bands, red bands, blue bands, green bands, and shortwave infrared bands of Landsat images.

For each pixel, the water frequency (WF) can be calculated as follows:

$$\text{WF} = \frac{1}{N} \sum_{i=1}^N w \quad (4)$$

where N represents the number of good-quality observations within one year, w is a binary variable that indicates the pixel type, with 1 for water bodies and 0 for non-water bodies. The value of WF ranges from 0 to 1.0. Previous studies have considered that when the annual WF of a pixel is equal to or greater than 0.25, it is classified as an annual effective water body [32,49]. In order to effectively reflect the long-term annual changes of surface water bodies in a specific region, the waters in the study refer to effective water bodies.

The extraction of surface water bodies is implemented on the GEE platform. First, this study selects the Landsat satellite series on the GEE platform across the Yellow River Basin during the period of 1986–2021. Each image undergoes cloud, shadow, and snow removal using the CFmask algorithm based on the quality assessment band (QA) of Landsat satellite datasets. NASADEM is utilized to calculate the slope. Since pixels with a slope exceeding 10° usually contain mountain shadows that may interfere with water pixels, these pixels are filtered out [7]. Second, surface water bodies are extracted using the criteria of ((MNDWI > EVI or MNDWI > NDVI) and (EVI < 0.1)). Pixels that meet the criteria are identified as water pixels and assigned a 1; otherwise, the pixels are identified as non-water pixels and assigned a 0. Third, the WF is calculated iteratively based on all water pixels in one year, and when $\text{WF} \geq 0.25$, the pixels are classified as annual surface water bodies. Fourth, based on the HydroLAKES and CRD dataset, lake masks and reservoir masks are generated by the 600 m buffer distance to include all possible historical water coverage scenarios [50], and surface water bodies are intersected with the lake and reservoir masks to generate the Natural Lake dataset and the Artificial Reservoir dataset, respectively. Finally, count the extraction results of surface water bodies in the Yellow River Basin every year and analyze the annual variation of the total water area, natural lake areas, and artificial reservoir areas. The workflow of surface water body extraction is shown in Figure 3.

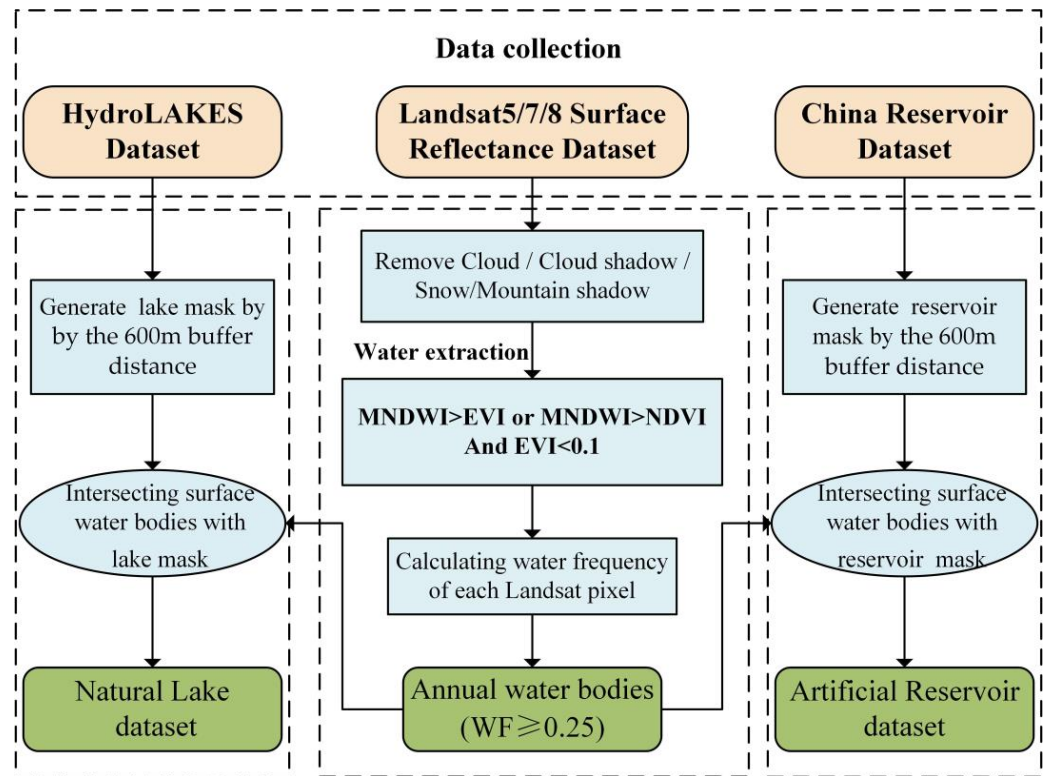


Figure 3. Flowchart of surface water extraction algorithm based on Landsat images.

2.3.2. Accuracy Assessment

To validate the accuracy of the water extraction results, a total of 8000 samples, including 4305 water samples and 3695 non-water samples, are generated using visual interpretation in Sentinel-2 images (Figure 4). Accuracy indices are used, including overall accuracy (OA), producer's accuracy (PA), user's accuracy (UA), and Kappa coefficient (Kc), which are based on confusion matrices. In addition, Sentinel-2 imagery and Landsat imagery should have the same date to minimize possible bias due to time differences, and a total of 138 Sentinel-2 images covering the entire YRB are used. The formulas for OA, PA, UA, and Kc are as follows:

$$\text{Overall accuracy} = \frac{p_{\text{Total}}}{N} \times 100\% \quad (5)$$

$$\text{Producer's accuracy} = \frac{p_{ij}}{p_i} \times 100\% \quad (6)$$

$$\text{User's accuracy} = \frac{p_{ij}}{p_j} \times 100\% \quad (7)$$

$$\text{Kappa coefficient} = \frac{N \times p_{\text{Total}} - \sum_{i=1}^r p_i p_j}{N^2 - \sum_{i=1}^r p_i p_j} \quad (8)$$

where p_{Total} represents the sum of correct classifications, N represents the sum of validation samples, r represents the number of rows in the confusion matrix, p_{ij} represents the number of observations in row i and column j in the confusion matrix; p_i represents a marginal total of row i ; p_j represents a marginal total of column j in the confusion matrix.

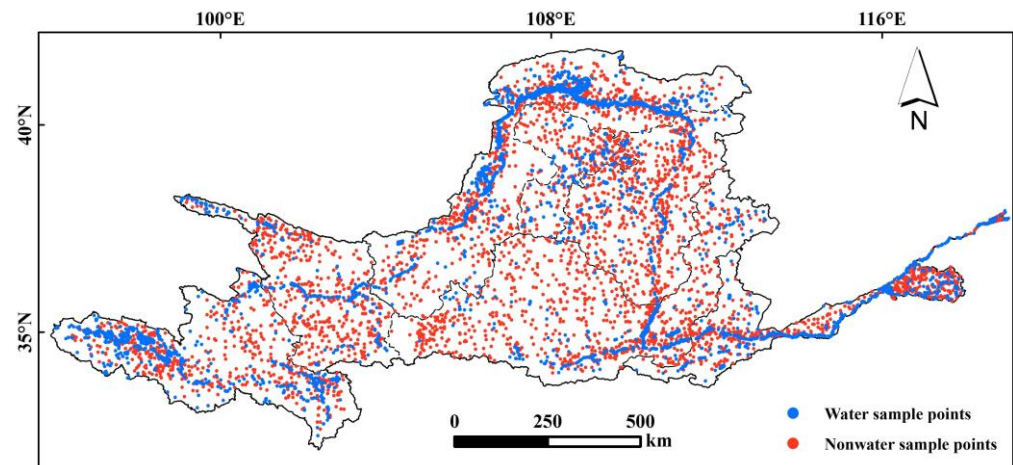


Figure 4. Spatial distribution of validation samples for water extraction results in the study.

2.3.3. Trend Analysis Methods

The trend analysis methods of Sen's slope [51] and the Mann–Kendall test [52,53] were used to discover trends in surface water bodies' area and climate factors. The methods have the advantage of being insensitive to outliers and have been used widely to detect temporal trends in hydrological and meteorological data. Sen's slope can be calculated as follows:

$$\text{Slope} = \text{median} \frac{x_j - x_i}{j - i} (1 < i < j) \quad (9)$$

where *slope* represents the inter-annual trend in surface water bodies, x_i and x_j represent the annual surface water bodies in i and j , respectively, and n is the length of the time series.

Mann–Kendall test can be calculated as follows:

$$S = \sum_{i=1}^{n-1} \sum_{k=i+1}^n \text{sgn}(x_k - x_i) \quad (10)$$

where x_k and x_i represent the continuous surface water bodies area variable, and n is the length of the time series.

$$\text{sgn}(\theta) = \begin{cases} 1, \theta > 0 \\ 0, \theta = 0 \\ -1, \theta < 0 \end{cases} \quad (11)$$

$$Z = \begin{cases} \frac{S-1}{\sqrt{\text{var}(S)}}, S > 0 \\ 0, S = 0 \\ \frac{S+1}{\sqrt{\text{var}(S)}}, S < 0 \end{cases} \quad (12)$$

When $|Z| > 1.96$, the variable has a significant level at the confidence level $p = 0.05$, and when $|Z| > 2.57$, the variable has a significant level at the confidence level $p = 0.01$.

2.3.4. Driving Factors of Surface Water Bodies Area Changes

The partial correlation coefficient was used to analyze the relationship between the surface water area of YRB and factors such as precipitation, air temperature, evaporation, and reservoir construction. It can reflect the degree of net correlation between two variables by analyzing the correlation between two variables only under the condition of controlling the linear influence of other variables. The greater the absolute value of the partial correlation coefficient (the closer it is to 1), the higher the degree of linear correlation between variables, and vice versa.

Multiple linear regression and contribution analysis [33] were used to quantify the contributions of meteorological factors and reservoir construction on the change in surface

water bodies area. To address the overestimation of the regression coefficients caused by the co-trendiness of the time-series data, this study first de-trended the surface water bodies area and the influencing factors. The regression coefficients were then calculated using multiple regression analysis (Equation (13)).

$$det_{SWA} = S_{Pre} \times det_{Pre} + S_{Tem} \times det_{Tem} + S_{Eva} \times det_{Eva} + S_{Rse} \times det_{Rse} \quad (13)$$

where det_{SWA} , det_{Pre} , det_{Tem} , det_{Eva} , and det_{Rse} represent the time series of surface water bodies area, precipitation, temperature, water surface evaporation, and reservoir construction after de-trending, respectively; S_{Pre} , S_{ET} , S_{Tem} , S_{Eva} , and S_{Rse} represent the regression coefficients of surface water bodies area, precipitation, temperature, water surface evaporation, and reservoir construction, respectively.

The contribution of single factors to the change in surface water bodies area can be calculated as follows:

$$\frac{d_{SWA}}{dt} = S_{Pre} \times \frac{d_{Pre}}{dt} + S_{Tem} \times \frac{d_{Tem}}{dt} + S_{Eva} \times \frac{d_{Eva}}{dt} + S_{Rse} \times \frac{d_{Rse}}{dt} \quad (14)$$

$$p(x) = \frac{\left| S_x \times \frac{d_x}{dt} \right|}{\left| S_{Pre} \times \frac{d_{Pre}}{dt} \right| + \left| S_{Tem} \times \frac{d_{Tem}}{dt} \right| + \left| S_{Eva} \times \frac{d_{Eva}}{dt} \right| + \left| S_{Res} \times \frac{d_{Res}}{dt} \right|} \quad (15)$$

where $\frac{d_{SWA}}{dt}$, $\frac{d_{Pre}}{dt}$, $\frac{d_{Tem}}{dt}$, $\frac{d_{Eva}}{dt}$, $\frac{d_{Rse}}{dt}$ represent the long-term trend of surface water bodies area, precipitation, temperature, water surface evaporation, and reservoir construction after de-trending, respectively, $p(x)$ is the contribution of single factors on the change in surface water bodies area.

3. Results

3.1. Accuracy Assessment of Surface Water Bodies

As shown in Table 1, the OA of the water extraction algorithm is 97.80%, the Kc is 0.96, the PA is 97.56%, and the UA is 98.37%, indicating that the surface water information extracted from Landsat images exhibits high accuracy and can be used for subsequent research.

Table 1. Accuracy assessment of surface water extraction algorithm used in the study.

Sample Number	Sample Number		Total	UA
	Water	Non-Water		
Water	4235	70	4305	98.37%
Non-Water	106	3589	3695	97.13%
Total	4573	3659		OA = 97.80%
PA	97.56%	98.09%		Kc = 0.96

3.2. The Areas of Surface Water Bodies and Spatial Distribution

Overall, from 1986–2021, the total water area (TWA) in the YRB is 9549.3 km² on average, accounting for 1.2% of the total area of the YRB. Among them, the average of natural lake areas (NLA) and artificial reservoir areas (ARA) are 2527.9 km² and 1871.7 km², respectively, accounting for 26.4% and 19.6% of the TWA in the YRB.

As shown in Table 2, the ULG sub-basin exhibits the largest total water area (TWA) of 2963.6 km², accounting for 31.0% of the total water area of YRB, followed by LTH (2824.0 km², 29.6%). The smallest TWA of 408.4 km², amounting to 4.2% of the YRB's total water area, is found in the IDA sub-basin. Similarly, the ULG sub-basin is the primary location for natural lakes and artificial reservoirs. The ULG has the largest NLA, covering a total area of 1772.3 km², accounting for 70.1%, while the STH sub-basin has the smallest

NLA, about 3.4 km², accounting for just 0.1% of TWA of the YRB. As for artificial reservoirs, the ULG also exhibits the largest area with 444.9 km² (23.7%), while the smallest is in IDA, with a total area of 16.5 km², accounting for only 0.9%.

Table 2. The average surface water bodies' area and proportion of the YRB and its sub-basins in 1986–2021. TWA is the total area of surface water bodies, NLA is the area of natural lakes, and ARA is the area of artificial reservoirs.

	TWA (km ²)	NLA (km ²)/ Proportion of TWA (%)	ARA (km ²)/ Proportion of TWA (%)
YRB	9549.5	2528.0/26.5	1871.7/19.6
ULG	2963.6	1772.3/59.8	444.9/15.0
LTL	531.9	21.1/4.0	310.9/58.5
IDA	408.4	187.9/46.0	16.5/4.0
LTH	2824.0	303.1/10.7	288.1/10.2
HTL	498.5	13.5/2.7	129.5/26.0
LTS	893.6	64.0/7.2	314.4/35.2
STH	495.1	3.4/0.7	274.2/55.4
LOH	934.4	162.7/17.4	93.2/10.0

The spatial distribution of different types of surface water bodies in the YRB varies significantly along longitude (Figure 5a) and latitude (Figure 5b). Natural lakes are mainly distributed in the ULG sub-basin (longitude less than 100°E), accounting for more than 90% of the total water area (Figure 5a). Large reservoirs are mainly distributed in the LTL and LTH sub-basin (longitude between 100–106°E), as well as downstream areas of the Yellow River. The remaining areas mainly consist of the Yellow River and its tributaries and scattered reservoirs. As the main water supply, many reservoirs are concentrated in urban areas.

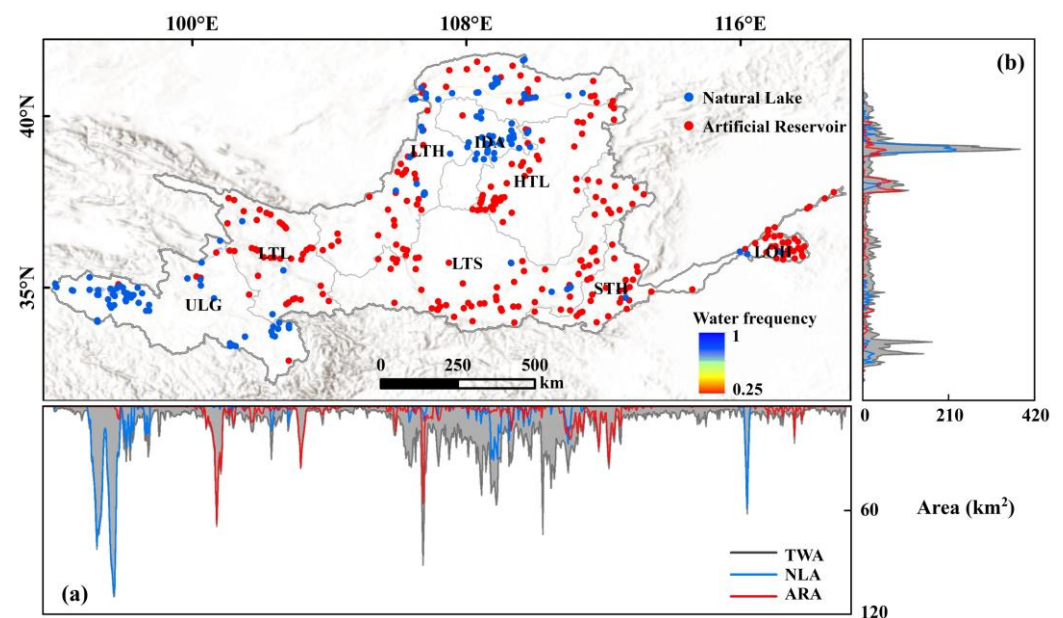


Figure 5. The spatial contribution of the average surface water bodies' area of the YRB in 1986–2021. The changes of surface water bodies area, including lakes and reservoirs, along with (a) latitude and (b) longitude.

The WF varies with season across the YRB (Figure 6a). The water pixels with $WF \geq 0.9$ are areas with water all year round, covering an extent of 2736.2 km², accounting for 49.3% of TWA, and consisting mainly of large lakes (such as Gyaring Lake and Ngoring Lake)

(Figure 6b,c), reservoirs (such as Liujiaxia Reservoir) (Figure 6d) and the mainstream of the Yellow River (Figure 6e,f). The area of water pixels with a WF of 0.25–0.3 is 1132.6 km², which is a seasonal variation of water bodies, mainly composed of small ponds, edges of rivers and lakes, and narrow streams. Due to fluctuations in water levels caused by seasonal changes, the extent of some water bodies may experience a reduction in their central areas during the dry season (Figure 6e). The higher the WF in water bodies, the higher the probability that these surface water bodies have a year-round continuous water surface. Conversely, the water bodies with lower WF may be affected by reduced precipitation or increased water consumption in some years.

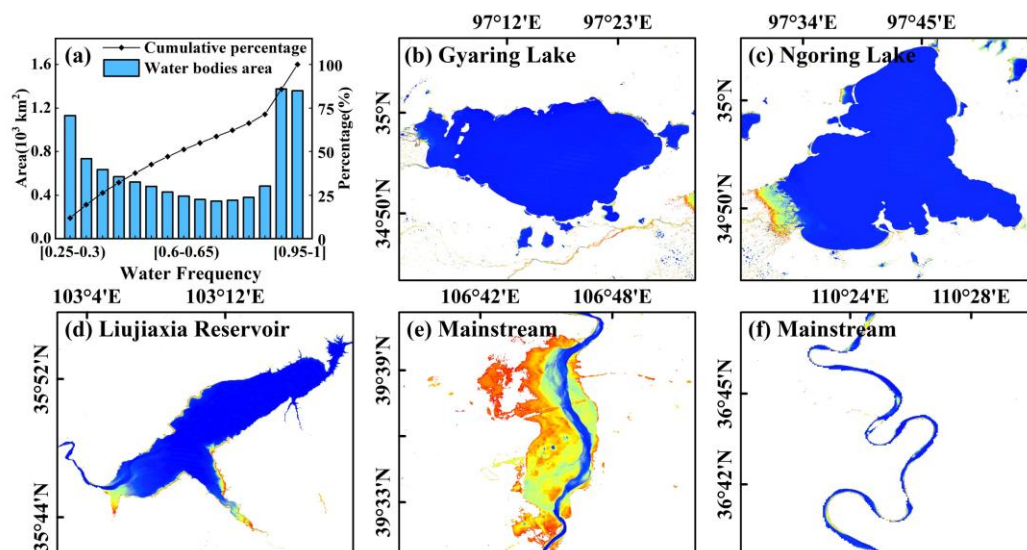


Figure 6. Maps of water frequency (WF) in the YRB during the period of 1986–2021. (a) Areas of surface water bodies at different levels of water frequency (0.05 intervals). Water frequency mapping of (b) Gyaring Lake, (c) Ngoring Lake, (d) Liujiaxia Reservoir, (e) mainstream of the Yellow River in the LTH sub-basin, and (f) mainstream of the Yellow River in HTL sub-basin, respectively.

3.3. Areal Changes of Surface Water Bodies

3.3.1. Annual Trends of Surface Water Bodies Area from 1986 to 2021

The TWA in the YRB, including NLA and ARA, has shown an overall significant upward trend ($p < 0.01$) (the p is calculated using the Mann–Kendall test) during the period of 1986–2021 (Figure 7a). TWA, NLA, and ARA have increased from 7392.0 km², 2445.4 km², and 1000.6 km² in 1986 to 10,375.8 km², 2726.6 km², and 2018.1 km² in 2021, an increase of 40.4%, 11.5% and 101.7%, respectively. The growth rate of ARA (21.6 km² yr⁻¹) in YRB is notably higher than that of NLA, which is 3.5 times faster than NLA (6.1 km² yr⁻¹).

The surface water bodies are divided into three types according to their area: small (1–10 km²), medium (10–50 km²), and large (more than 50 km²), and the changes in the area and number of surface water bodies of these three levels are analyzed in 1986–2021 (Figure 7b–d).

Small-size natural lakes and artificial reservoirs show an upward trend in both area and number (Figure 7b). The NLA and ARA increased from 267.1 km² and 274.1 km² in 1986 to 347.5 km² and 470.3 km², an increase of 30.1% and 71.6%, respectively, and the number of natural lakes and artificial reservoirs increased by 16 and 75, respectively. The areas of medium (Figure 7c) and large-sized (Figure 7d) artificial reservoirs increased significantly, increasing by 224.5 km² (101.7%) and 596.8 km² (118.0%), respectively, while natural lakes changed less, increasing by 40.5 km² (8.6%) and 160.3 km² (9.6%), respectively.

The annual fluctuations of NLA and ARA are not completely consistent, especially during the severe drought in YRB in 1989 (Figure 7c,d). The areas of medium and large-sized natural lakes decreased significantly, while the areas of artificial reservoirs increased

instead of decreasing. Water storage projects may affect or even reverse the natural trend of changes in the areas of artificial water bodies.

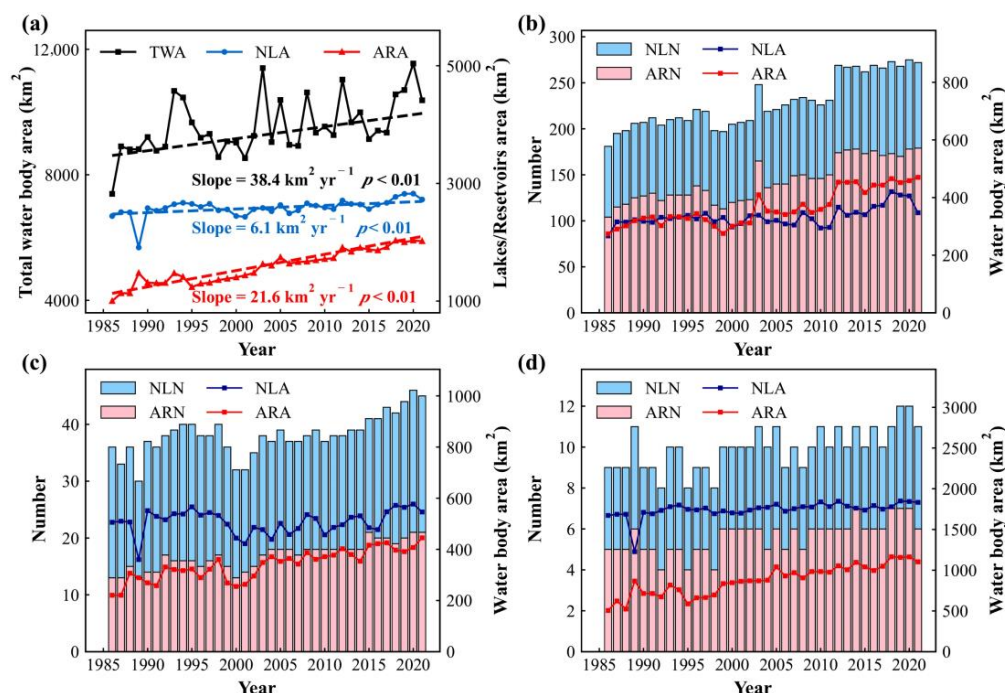


Figure 7. Annual variation of surface water bodies from 1986 to 2021. (a) The trends of TWA, NLA, and ARA in the YRB. The trend is determined using Mann–Kendall, and the rate is calculated using Sen’s slope. The changes in the number and area of natural lakes and artificial reservoirs in different area levels: (b) 1 to 10 km²; (c) 10 to 50 km²; (d) greater than 50 km². NLN and ARN refer to the number of natural lakes and artificial reservoirs; NLA and ARA refer to the area of lakes and reservoirs.

3.3.2. Spatial Distribution of the Trend of Surface Water Area

As shown in Figure 8a, except for IDA (TWA decreased by 38.0 km²), the TWA changes in all other sub-basins of YRB exhibited a positive increasing trend during the period of 1986–2021. Among them, the TWA of LTH and ULG increased obviously, which were 1321.8 and 724.8 km², an increase of 70.6% and 28.5%, respectively. Similar to the TWA, the changes in NLA within YRB were mostly positive, except for sub-basin IDA. Among them, LTH and ULG had the largest increase in NLA, with an increase of 146.8 km² and 123.9 km², respectively. The difference is that the changes in the area of artificial reservoirs in all sub-basins showed a net increase. The ULG sub-basin had the largest increase in ARA at 343.6 km², followed by STH with a total of 258.0 km², and IDA had the smallest increase in ARA at 4.5 km².

The number of natural lakes that have significantly expanded and shrunk was counted. A total of 102 natural lakes in YRB expanded in size, and 23 natural lakes shrunk. Most of the natural lakes in the upper YRB are expanding significantly, such as ULG (100%) and LTH (86.5%), while most of the shrinking natural lakes are located in IDA (51.9%). In YRB, there are 22 natural lakes with an expansion area of more than 3 km², seven natural lakes with an expansion area of more than 10 km², and one with an expansion area of more than 50 km², such as Ngoring Lake (Figure 8b) in ULG, with an expansion area of 61.0 km². There are 25 natural lakes with a shrinking area of less than 5 km², of which Hongjiannao Lake (Figure 8c) has the largest shrinking area, about 20.1 km².

In the YRB, 204 artificial reservoirs were significantly expanded, and 77 shrunk. The expansion changes of artificial reservoirs were mainly concentrated in LTS (81.8%) and LTH (82.0%), while the artificial reservoirs in the middle and lower reaches of YRB shrank more, such as HTL (46.5%) and LOH (50.0%). There are 36 artificial reservoirs with an

expansion area of more than 3 km², of which 13 are expanded over 10 km², and three are expanded over 50 km². The artificial reservoir with the largest expansion area is Longyangxia Reservoir (Figure 8d) in ULG, with an expansion area of 319.2 km². The shrinking area of 75 artificial reservoirs is less than 5 km², among which Sanshenggong Reservoir (Figure 8e) has the largest shrinking area, about 20.5 km².

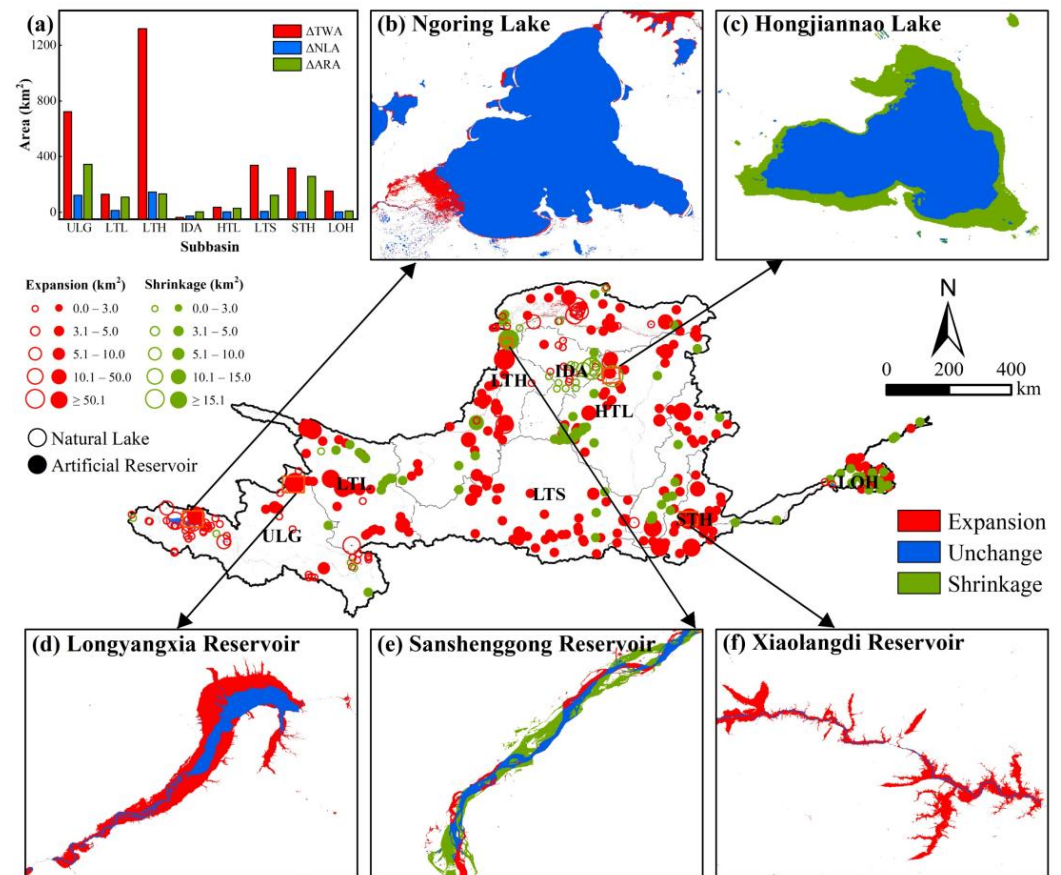


Figure 8. Expansion and shrinkage of surface water bodies from 1986 to 2021 in the YRB. (a) The area changes of surface water bodies, lakes, and reservoirs in eight sub-basins. The expansion and shrinkage of surface water bodies of (b) Noring Lake, (c) Hongjiannao Lake, (d) Longyangxia Reservoir, (e) Sanshenggong Reservoir, and (f) Xiaolangdi Reservoir, respectively.

3.4. Drivers of Surface Water Bodies Area Changes

Partial correlation analysis was used to study the influence of meteorological factors and reservoir construction on the surface water bodies area of different sub-basins (Figure 9). Except for IDA ($R = 0.24$, $p = 0.17$), precipitation was the dominant climatic factor for surface water changes in the remaining seven sub-basins of the YRB. There was a strong and significant positive correlation between surface water bodies' area change and precipitation ($p < 0.05$) (Figure 9a). The increase in temperature had a significant positive correlation with the expansion of water area in alpine regions, such as ULG ($R = 0.47$, $p < 0.01$) and LTL ($R = 0.42$, $p < 0.05$) in the upper reaches of the Yellow River (Figure 9b). The effect of evaporation on surface water bodies area was weak, and only one sub-basin STH ($R = -0.44$, $p < 0.05$) showed a significant negative correlation between surface water bodies area changes and evaporation (Figure 9c). The partial correlations in the IDA between surface water bodies' area changes and precipitation, temperature, and evaporation were found to be weak (p -precipitation, p -temperature, and p -evaporation were all greater than 0.15). In addition, except for LTL ($R = 0.31$, $p = 0.06$), the remaining seven sub-basins showed a significant positive correlation between surface water bodies area changes and reservoir construction (Figure 9d).

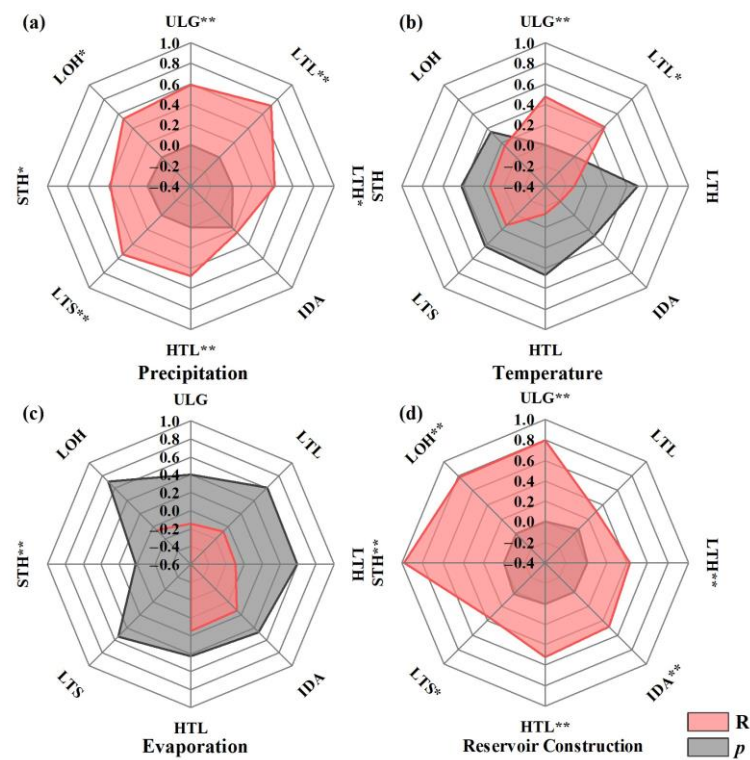


Figure 9. Partial correlation coefficient between (a) precipitation, (b) temperature, (c) water evaporation, reservoir construction (d) and surface water bodies area in individual sub-basin with different significance levels. (* $p < 0.05$ and ** $p < 0.01$).

The result of contribution analysis showed that the combined contribution of meteorological factors on surface water bodies area variation was 67.4% in the whole YRB, and the remaining 32.6% of the variation in surface water bodies area is attributed to reservoir construction.

Among the meteorological factors, precipitation accounts for 47%, temperature for 16%, and water surface evaporation for 4.4%. In specific sub-basins within the YRB, precipitation has the greatest influence on changes in surface water bodies area, exceeding 50% in the IDA (78.5%), LTS (76.4%), LTH (71.6%), and LTL (65.6%). These sub-basins are primarily affected by precipitation patterns. Contrarily, temperature contributes less than 10% in the six remaining sub-basins, except for LTL (24.7%) and ULG (22.7%). Surface water evaporation has a relatively minor impact on changes in surface water bodies area (Figure 10a–c).

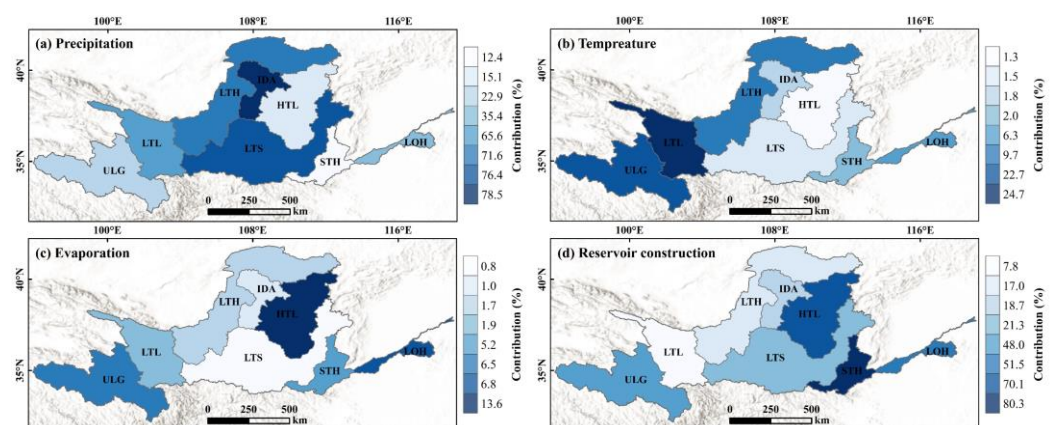


Figure 10. Contributions of precipitation (a), temperature (b), evaporation (c), and reservoir construction (d) to surface water bodies area changes in eight sub-basins of the Yellow River Basin.

Since the 1980s, the Yellow River Basin has vigorously built reservoirs, with more than 70 reservoirs continuously increasing. From 1986 to 2021, 32.6% of the change in surface water bodies area in the YRB was caused by artificial reservoirs. In the STH (80.3%), HTL (70.1%), and STH (51.5%) sub-basins, reservoir construction dominates changes in surface water bodies area (Figure 10d). As for HTL sub-basin, the area of artificial reservoirs in this sub-basin accounts for 26% of the total water area, but 70.1% of the increase in water area is caused by the expansion of artificial reservoirs. In the ULG sub-basin, the contribution of reservoir construction to the change in surface water bodies area was 48%, but the expansion of Longyangxia Reservoir, a large reservoir built in 1986 and surged in 1987, accounted for 92.9% (319.2 km²) of the change in the reservoir area.

4. Discussion

4.1. Impact of Climate and Human Activities on Changes in Surface Water Bodies

Climate change is one of the most important impacts on global water and ecosystems. As has been observed in recent decades, key hydrological and physical variables such as surface temperature, evapotranspiration, and land cover all respond dramatically and rapidly to climate change [54]. Over the past three decades, more than 90,000 km² of surface water bodies came into existence globally [31], and associated expansion hotspots were identified in regions that are less affected by human activities, such as the Qinghai-Tibet Plateau, Greenland, and the Rocky Mountains [55]. The opposite results were also observed in southern Australia, western USA, central Asia, and the Middle East, where the area of surface water bodies decreased, which was associated with local drought events [56,57].

This study has found that the total water area in the YRB showed an obvious upward trend from 1986 to 2021, an increase of 40.4% ($p < 0.05$) (Figure 8a). Climate change has contributed over 60% to this increase in surface water bodies area. Precipitation plays an important role as a source of surface water in the YRB. The precipitation in the YRB exhibits a clear upward trend (Table 3), which can directly increase the quantity and area of surface water bodies. This study confirmed a significant and positive correlation between the change in surface water bodies area and annual precipitation in the YRB (Figure 9a). The increased precipitation mostly drove the expansion of non-glacial lakes, which is consistent with previous findings [58]. Localized studies have also demonstrated that changes in non-glacial lakes were dominated by precipitation, such as the middle and lower reaches of the Yangtze River Basin, including Taihu Lake, Poyang Lake, and Dongting Lake [59,60]. The increase in temperature exhibits a significant and positive correlation with the expansion of water area in alpine regions, such as the ULG and LTL (Figure 9b). These regions are situated on the Qinghai-Tibet Plateau, which has an average elevation exceeding 3500 m and have experienced an annual temperature increase of approximately 1.8 °C, surpassing the global warming rate. Warming temperatures have accelerated the melting of glaciers, snow, and permafrost at the source of the Yellow River, increasing the amount of runoff into the lakes and indirectly contributing to the expansion of the lakes [61]. Moreover, as a major contributor to terrestrial water depletion, the decline in evaporation may have also played a role in mitigating water scarcity [62].

Human activities, such as reservoir construction, are an important factor affecting changes in the surface water bodies area [31,63]. The construction of reservoirs is mainly used for various human water needs, including domestic water, industrial water, and irrigation water, and it can directly increase the quantity and area of surface water bodies [42,64]. Our study shows that 32.6% of the area change of surface water bodies in the YRB is attributable to artificial reservoirs during the period of 1986–2021. In the STH and HTL sub-basins, artificial reservoirs contributed more than 70% to the increase in surface water bodies area (Figure 10).

Table 3. Annual trends of climatic variables, precipitation, temperature, and evaporation, in the Yellow River Basin and its sub-basins from 1986 to 2021. A single asterisk indicates a significance level of 0.05, and a double asterisk indicates a significance level of 0.01.

	Precipitation (mm yr ⁻¹)	Temperature (°C yr ⁻¹)	Evaporation (mm yr ⁻¹)
YRB	3.85 **	0.04 **	−0.35
ULG	5.97 **	0.03 **	0.40 *
LTL	3.75 **	0.04 **	0.31 *
IDA	2.41 **	0.03 **	−1.41
LTH	2.48 *	0.03 **	−1.33
HTL	4.44 **	0.04 **	−0.78
LTS	4.46 **	0.03 **	−0.16
STH	4.01 *	0.04 **	−0.15
LOH	3.50	0.03 **	−0.23

4.2. Performance and Uncertainty of Water Extraction Algorithms

This study assessed the practical applicability of the algorithm in different regions, including the United States, Brazil, Germany, South Africa, Russia, and Australia (Figure 11), and verified the accuracy of water body extraction results. These countries exhibit significant differences in terms of climate conditions, geomorphic features, land use, and water body sizes, which could potentially impact the accuracy of water body extraction. The research findings indicate that this method consistently achieves high accuracy, typically exceeding 96% (Table 4). Previous studies have shown that the algorithm achieves high accuracy, generally above 90% [65]. In this study, the water body extraction results in the YRB achieved high accuracy (97.8%). This suggests that changes in external environmental conditions have a relatively minor impact on the algorithm's practicality. Therefore, there is substantial potential for the algorithm's widespread use in other regions.

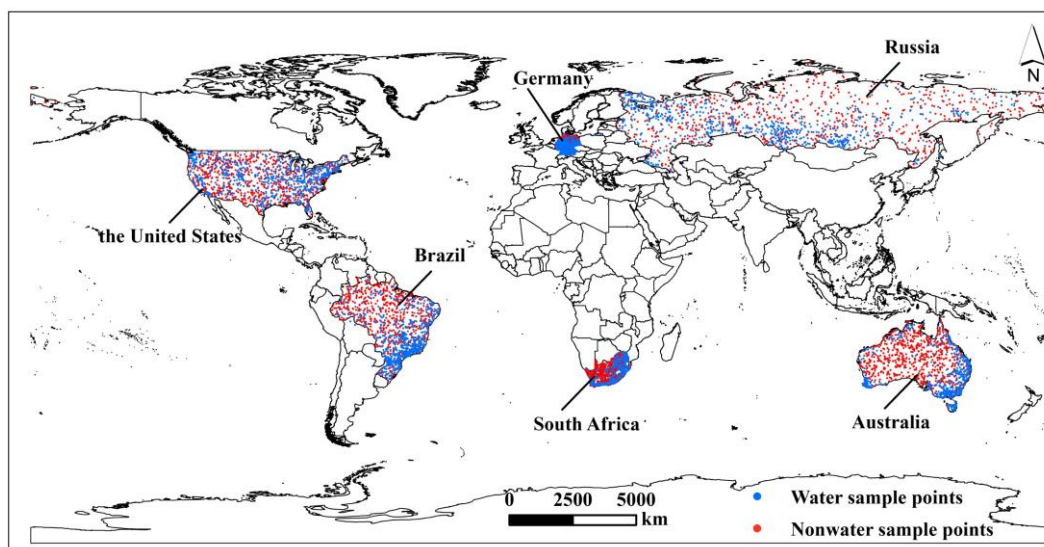


Figure 11. Validation samples for water extraction results in the United States, Brazil, Germany, South Africa, Russia, and Australia.

The surface water dataset of this study and the JRC data are compared to quantify their differences and similarities. Overall, the two products are relatively consistent in terms of spatial distributions and patterns of water bodies boundaries. However, the JRC data sometimes misses water bodies, resulting in discontinuities in river network connectivity. As shown in Figure 12h,i,l, in the JRC data, the WF of the mainstream of the Yellow River is mostly around 0.60, which is inconsistent with the reality that there was no break in the

mainstream of the Yellow River in 2019. Other studies have shown that JRC data has large omissions in the identification of water bodies in summer, resulting in lower WF [37].

Table 4. The surface water extraction accuracy in the Yellow River basin and other region.

Regions	OA	Kc
The United State	97.12%	0.94
Brazil	96.25%	0.93
Germany	97.80%	0.96
South Africa	96.57%	0.93
Russia	96.11%	0.93
Australia	97.01%	0.94
The Yellow River Basin	97.80%	0.96

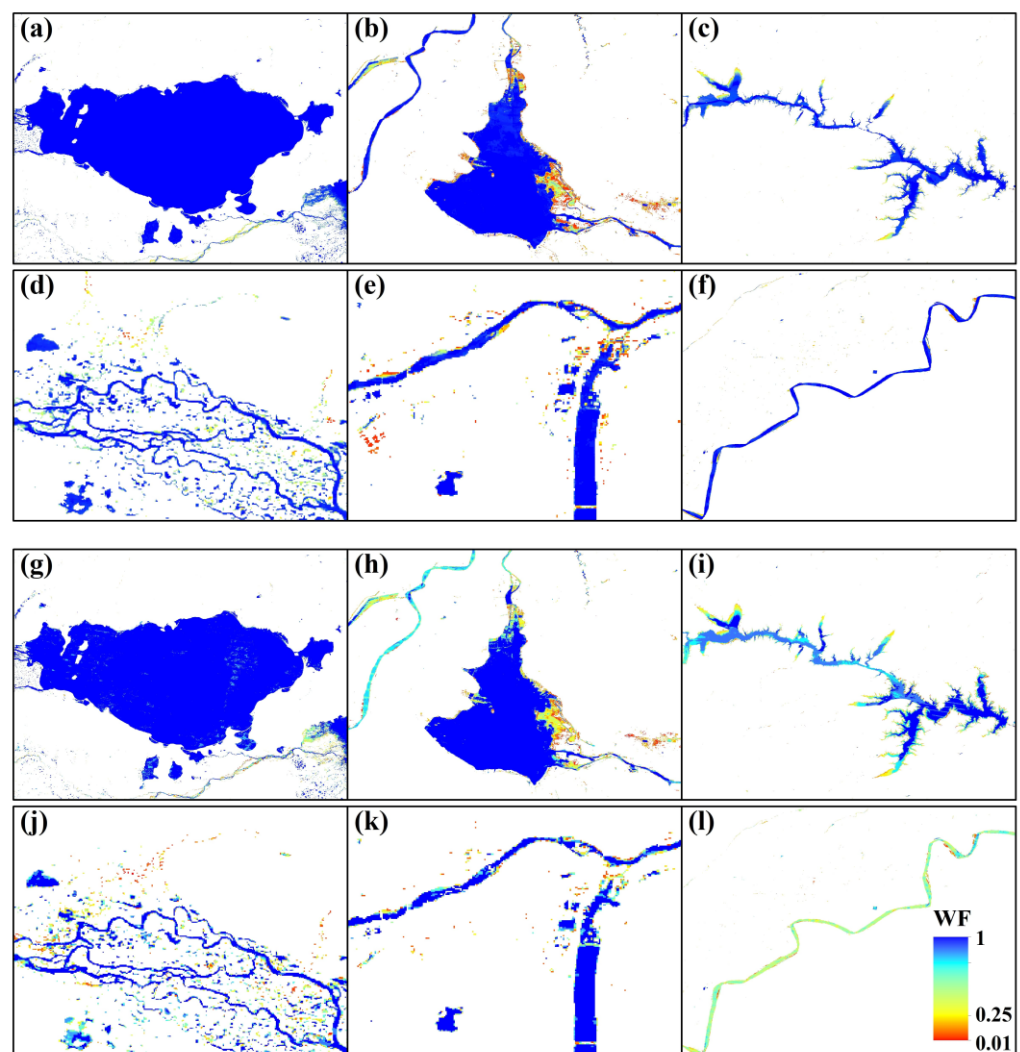


Figure 12. Comparison of water frequency maps between the study (a–f) and JRC dataset (g–l). (a,g) Gyaring Lake, (b,h) Dongping Lake, (c,i) Xiaolangdi Reservoir, (d,j) mountainous water bodies in ULG, (e,k) urban water bodies in Xi'an City, and (f,l) mainstream in the lower reaches of the Yellow River, respectively.

Due to the impact of image data resolution and the environmental conditions, there are still some limitations or uncertainties in the accuracy of the surface water bodies dataset in this study. First of all, due to the limitation of spatial resolution of remote sensing data, water bodies smaller than 900 m² cannot be identified. Second, the accuracy of

water extraction results may be reduced due to ice and snow cover in some months [66]. Finally, due to the 16-day revisit period of Landsat imagery, omission errors are inevitable when observations do not coincide with some short-term events in surface water, such as floods [67]. The Landsat image quantity and data quality need attention in follow-up research.

5. Conclusions

This study explores the temporal and spatial dynamics of surface water bodies area in the YRB and its eight sub-basins and quantitatively evaluates the driving factors of the area changes in the surface water bodies area. It was found that the TWA, NLA, and ARA in the YRB increased by 2983.8 km² (40.4%), 281.1 km² (11.5%), and 1017.6 km² (101.7%), respectively. The results reveal a continuing upward trend in the total area of surface water bodies in the YRB, expanding at a rate of 38.4 km² yr⁻¹. Notably, the rate of increasing artificial reservoir areas was much greater than that of natural lakes. The increasing precipitation can directly increase the area and number of surface water bodies, and it largely contributed to the net volume increase in surface water bodies area, counting for 47%. Human activities, such as reservoir construction and water storage, contributed 32.6% to the change of surface water area, especially in the HTL, LTL, and STH sub-basins. Additionally, the rising temperature (contributed 22.7% to the change of surface water area) has accelerated the melting of permafrost and ice and snow in the source of the YRB, increasing the amount of runoff into the lakes, which indirectly led to the significant expansion of surface water bodies, especially the natural lakes. The decline in evaporation has played a role in mitigating water scarcity.

The water extraction process constructed in this study reduces the large uncertainties introduced in previous efforts to use date-specific images in different years. This automated process uses open data and cloud-based platforms for analysis, so it is suitable for water monitoring in various other regions, and the advent of other sensors with higher spatiotemporal resolution (e.g., Worldview 4, Sentinel-2) will further help improve surface water bodies extraction in the future. The results of this study provide an important reference for the meticulous management and optimal allocation of water resources under the circumstances of climate change and intensified human activities.

Author Contributions: Conceptualization, Z.Z. and H.L.; methodology, Z.Z. and H.L.; validation, Z.Z., H.L. and X.S.; formal analysis, Z.Z. and H.L.; investigation, Z.Z., X.S. and W.S.; resources, Z.Z. and W.S.; data curation, Z.Z. and H.L.; writing—original draft preparation, Z.Z., X.S. and W.S.; writing—review and editing, Z.Z., X.S. and W.S.; visualization, Z.Z. and H.L.; supervision, X.S. and W.S.; project administration, X.S. and W.S.; funding acquisition, X.S. and W.S. All authors have read and agreed to the published version of the manuscript.

Funding: This research was funded by the National Key Research and Development Program of China (Grant Number: 2022YFC3201702), the National Natural Science Foundation of China (Grant Number: 42177328) and Western Young Scholars of the Chinese Academy of Sciences (Grant Number: XAB2022YW02).

Data Availability Statement: The data are not publicly available due to privacy restrictions.

Conflicts of Interest: The authors declare no conflict of interest.

References

1. McDonald, R.I.; Weber, K.; Padowski, J.; Flörke, M.; Schneider, C.; Green, P.A.; Gleeson, T.; Eckman, S.; Lehner, B.; Balk, D. Water on an urban planet: Urbanization and the reach of urban water infrastructure. *Glob. Environ. Chang.* **2014**, *27*, 96–105.
2. Suring, L.H. Freshwater: Oasis of Life—An Overview. In *Encyclopedia of the World's Biomes*; Elsevier: Oxford, UK, 2020; pp. 1–11.
3. Plessis, A.D. Freshwater and Industries. In *Encyclopedia of the World's Biomes*; Elsevier: Oxford, UK, 2020; pp. 55–62.
4. Edwards, E.C.; Nehra, A. Importance of Freshwater for Irrigation. In *Encyclopedia of the World's Biomes*; Elsevier: Oxford, UK, 2020; pp. 22–28.
5. Ren, L.; Wang, M.; Li, C.; Zhang, W. Impacts of human activity on river runoff in the northern area of China. *J. Hydrol.* **2002**, *261*, 204–217. [[CrossRef](#)]

6. Khandelwal, A.; Karpatne, A.; Marlier, M.E.; Kim, J.; Lettenmaier, D.P.; Kumar, V. An approach for global monitoring of surface water extent variations in reservoirs using MODIS data. *Remote Sens. Environ.* **2017**, *202*, 113–128.
7. Klein, I.; Gessner, U.; Dietz, A.J.; Kuenzer, C. Global WaterPack—A 250 m resolution dataset revealing the daily dynamics of global inland water bodies. *Remote Sens. Environ.* **2017**, *198*, 345–362.
8. Berge-Nguyen, M.; Cretaux, J.F. Inundations in the Inner Niger Delta: Monitoring and analysis using MODIS and global precipitation datasets. *Remote Sens.* **2015**, *7*, 2127–2151.
9. Mueller, N.; Lewis, A.; Roberts, D.; Ring, S.; Melrose, R.; Sixsmith, J.; Lymburner, L.; McIntyre, A.; Tan, P.; Curnow, S.; et al. Water observations from space: Mapping surface water from 25 years of Landsat imagery across Australia. *Remote Sens. Environ.* **2016**, *174*, 341–352. [[CrossRef](#)]
10. Yao, F.; Wang, J.; Wang, C.; Crétaux, J.-F. Constructing long-term high-frequency time series of global lake and reservoir areas using Landsat imagery. *Remote Sens. Environ.* **2019**, *232*, 111210. [[CrossRef](#)]
11. Feyisa, G.L.; Meilby, H.; Fensholt, R.; Proud, S.R. Automated Water Extraction Index: A new technique for surface water mapping using Landsat imagery. *Remote Sens. Environ.* **2014**, *140*, 23–35. [[CrossRef](#)]
12. Yamazaki, D.; Trigg, M.A.; Ikeshima, D. Development of a global similar to 90 m water body map using multi-temporal Landsat images. *Remote Sens. Environ.* **2015**, *171*, 337–351. [[CrossRef](#)]
13. Schwatke, C.; Scherer, D.; Dettmering, D. Automated Extraction of Consistent Time-Variable Water Surfaces of Lakes and Reservoirs Based on Landsat and Sentinel-2. *Remote Sens.* **2019**, *11*, 1010.
14. Steinhausen, M.J.; Wagner, P.D.; Narasimhan, B.; Waske, B. Combining Sentinel-1 and Sentinel-2 data for improved land use and land cover mapping of monsoon regions. *Int. J. Appl. Earth Obs. Geoinf.* **2018**, *73*, 595–604.
15. Jakovljevic, G.; Govedarica, M.; Alvarez-Taboada, F. Waterbody mapping: A comparison of remotely sensed and GIS open data sources. *Int. J. Remote Sens.* **2019**, *40*, 2936–2964.
16. Gómez, C.; White, J.C.; Wulder, M.A. Optical remotely sensed time series data for land cover classification: A review. *ISPRS J. Photogramm. Remote Sens.* **2016**, *116*, 55–72. [[CrossRef](#)]
17. Wang, Y.; Ma, J.; Xiao, X.; Wang, X.; Zhao, B. Long-Term Dynamic of Poyang Lake Surface Water: A Mapping Work Based on the Google Earth Engine Cloud Platform. *Remote Sens.* **2019**, *11*, 313. [[CrossRef](#)]
18. Halabisky, M.; Moskal, L.M.; Gillespie, A.; Hannam, M. Reconstructing semi-arid wetland surface water dynamics through spectral mixture analysis of a time series of Landsat satellite images (1984–2011). *Remote Sens. Environ.* **2016**, *177*, 171–183. [[CrossRef](#)]
19. Tedros, B.; Charles, L.; Wu, Q.; Bradley, A.; Oleg, A.; Victor, C.; Liu, H. Decision-Tree, Rule-Based, and Random Forest Classification of High-Resolution Multispectral Imagery for Wetland Mapping and Inventory. *Remote Sens.* **2018**, *10*, 580.
20. McFeeters, S.K. The use of the Normalized Difference Water Index (NDWI) in the delineation of open water features. *Int. J. Remote Sens.* **1996**, *17*, 1425–1432.
21. Xu, H. Modification of normalised difference water index (NDWI) to enhance open water features in remotely sensed imagery. *Int. J. Remote Sens.* **2006**, *27*, 3025–3033.
22. Tulbure, M.G.; Broich, M.; Stehman, S.V.; Kommareddy, A. Surface water extent dynamics from three decades of seasonally continuous Landsat time series at subcontinental scale in a semi-arid region. *Remote Sens. Environ.* **2016**, *178*, 142–157.
23. Otsu, N. A Threshold Selection Method from Gray-Level Histograms. *IEEE Trans. Syst. Man Cybern.* **2007**, *9*, 62–66. [[CrossRef](#)]
24. Yang, X.; Qin, Q.; Grussenmeyer, P.; Koehl, M. Urban surface water body detection with suppressed built-up noise based on water indices from Sentinel-2 MSI imagery. *Remote Sens. Environ.* **2018**, *219*, 259–270. [[CrossRef](#)]
25. Han, Q.; Niu, Z. Construction of the Long-Term Global Surface Water Extent Dataset Based on Water-NDVI Spatio-Temporal Parameter Sets. *Remote Sens.* **2020**, *12*, 2675. [[CrossRef](#)]
26. Gorelick, N.; Hancher, M.; Dixon, M.; Ilyushchenko, S.; Thau, D.; Moore, R. Google Earth Engine: Planetary-scale geospatial analysis for everyone. *Remote Sens. Environ.* **2017**, *202*, 18–27. [[CrossRef](#)]
27. Zurqani, H.A.; Post, C.J.; Mikhailova, E.A.; Schlautman, M.A.; Sharp, J.L. Geospatial analysis of land use change in the Savannah River Basin using Google Earth Engine. *Int. J. Appl. Earth Obs. Geoinf.* **2018**, *69*, 175–185. [[CrossRef](#)]
28. Chen, B.; Xiao, X.; Li, X.; Pan, L.; Doughty, R.; Ma, J.; Dong, J.; Qin, Y.; Zhao, B.; Wu, Z. A mangrove forest map of China in 2015: Analysis of time series Landsat 7/8 and Sentinel-1A imagery in Google Earth Engine cloud computing platform. *ISPRS J. Photogramm. Remote Sens.* **2017**, *131*, 104–120. [[CrossRef](#)]
29. Liu, X.; Hu, G.; Chen, Y.; Xia, L.; Pei, F. High-resolution multi-temporal mapping of global urban land using Landsat images based on the Google Earth Engine Platform. *Remote Sens. Environ.* **2018**, *209*, 227–239. [[CrossRef](#)]
30. Murray, N.J.; Phinn, S.R.; DeWitt, M.; Ferrari, R.; Johnston, R.; Lyons, M.B.; Clinton, N.; Thau, D.; Fuller, R.A. The global distribution and trajectory of tidal flats. *Nature* **2019**, *565*, 222–225. [[CrossRef](#)] [[PubMed](#)]
31. Pekel, J.F.; Cottam, A.; Gorelick, N.; Belward, A.S. High-resolution mapping of global surface water and its long-term changes. *Nature* **2016**, *540*, 418–422. [[CrossRef](#)] [[PubMed](#)]
32. Zou, Z.; Xiao, X.; Dong, J.; Qin, Y.; Doughty, R.B.; Menarguez, M.A.; Zhang, G.; Wang, J. Divergent trends of open-surface water body area in the contiguous United States from 1984 to 2016. *Proc. Natl. Acad. Sci. USA* **2018**, *115*, 3810–3815. [[CrossRef](#)]
33. Wang, X.; Xiao, X.; Zou, Z.; Dong, J.; Qin, Y.; Doughty, R.B.; Menarguez, M.A.; Chen, B.; Wang, J.; Ye, H.; et al. Gainers and losers of surface and terrestrial water resources in China during 1989–2016. *Nat. Commun.* **2020**, *11*, 3471. [[CrossRef](#)]

34. Xie, J.; Xu, Y.-P.; Wang, Y.; Gu, H.; Wang, F.; Pan, S. Influences of climatic variability and human activities on terrestrial water storage variations across the Yellow River basin in the recent decade. *J. Hydrol.* **2019**, *579*, 124218. [[CrossRef](#)]
35. Liu, Y.; Song, H.; An, Z.; Sun, C.; Trouet, V.; Cai, Q.; Liu, R.; Leavitt, S.W.; Song, Y.; Li, Q.; et al. Recent anthropogenic curtailing of Yellow River runoff and sediment load is unprecedented over the past 500 y. *Proc. Natl. Acad. Sci. USA* **2020**, *117*, 18251–18257. [[CrossRef](#)] [[PubMed](#)]
36. Şerban, R.D.; Jin, H.; Şerban, M.; Luo, D. Shrinking thermokarst lakes and ponds on the northeastern Qinghai-Tibet plateau over the past three decades. *Permafrost. Periglac. Process.* **2021**, *32*, 601–617. [[CrossRef](#)]
37. Zhou, H.; Liu, S.; Hu, S.; Mo, X. Retrieving dynamics of the surface water extent in the upper reach of Yellow River. *Sci. Total Environ.* **2021**, *800*, 149348. [[CrossRef](#)]
38. Wang, R.; Xia, H.; Qin, Y.; Niu, W.; Pan, L.; Li, R.; Zhao, X.; Bian, X.; Fu, P. Dynamic Monitoring of Surface Water Area during 1989–2019 in the Hetao Plain Using Landsat Data in Google Earth Engine. *Water* **2020**, *12*, 3010. [[CrossRef](#)]
39. Yan, D.; Wang, X.; Zhu, X.; Huang, C.; Li, W. Analysis of the use of NDWIGreen and NDWired for inland water mapping in the Yellow River Basin using Landsat-8 OLI imagery. *Remote Sens. Lett.* **2017**, *8*, 996–1005. [[CrossRef](#)]
40. Yang, D.; Li, C.; Hu, H.; Lei, Z.; Yang, S.; Kusuda, T.; Koike, T.; Musiaka, K. Analysis of water resources variability in the Yellow River of China during the last half century using historical data. *Water Resour. Res.* **2004**, *40*, W06502. [[CrossRef](#)]
41. Wang, W.; Shao, Q.; Peng, S.; Xing, W.; Yang, T.; Luo, Y.; Yong, B.; Xu, J. Reference evapotranspiration change and the causes across the Yellow River Basin during 1957–2008 and their spatial and seasonal differences. *Water Resour. Res.* **2012**, *48*, W05530. [[CrossRef](#)]
42. Song, C.; Fan, C.; Zhu, J.; Wang, J.; Sheng, Y.; Liu, K.; Chen, T.; Zhan, P.; Luo, S.; Yuan, C. A comprehensive geospatial database of nearly 100,000 reservoirs in China. *Earth Syst. Sci. Data* **2022**, *14*, 4017–4034. [[CrossRef](#)]
43. Xia, H.; Zhao, J.; Qin, Y.; Yang, J.; Cui, Y.; Song, H.; Ma, L.; Jin, N.; Meng, Q. Changes in Water Surface Area during 1989–2017 in the Huai River Basin using Landsat Data and Google Earth Engine. *Remote Sens.* **2019**, *11*, 1824. [[CrossRef](#)]
44. Huang, J.; Zhang, G.; Zhang, Y.; Guan, X.; Wei, Y.; Guo, R. Global desertification vulnerability to climate change and human activities. *Land Degrad. Dev.* **2020**, *31*, 1380–1391.
45. Li, Z.; Yan, Z.; Zhu, Y.; Freychet, N.; Tett, S. Homogenized daily relative humidity series in China during 1960–2017. *Adv. Atmos. Sci.* **2020**, *37*, 318–327.
46. Wang, X.; Xiao, X.; Zou, Z.; Chen, B.; Ma, J.; Dong, J.; Doughty, R.B.; Zhong, Q.; Qin, Y.; Dai, S.; et al. Tracking annual changes of coastal tidal flats in China during 1986–2016 through analyses of Landsat images with Google Earth Engine. *Remote Sens. Environ.* **2020**, *238*, 110987. [[CrossRef](#)] [[PubMed](#)]
47. Santoro, M.; Wegmuller, U.; Lamarche, C.; Bontemps, S.; Defoumy, P.; Arino, O. Strengths and weaknesses of multi-year Envisat ASAR backscatter measurements to map permanent open water bodies at global scale. *Remote Sens. Environ.* **2015**, *171*, 185–201. [[CrossRef](#)]
48. Dong, J.W.; Xiao, X.M.; Kou, W.L.; Qin, Y.W.; Zhang, G.L.; Li, L.; Jin, C.; Zhou, Y.T.; Wang, J.; Biradar, C.; et al. Tracking the dynamics of paddy rice planting area in 1986–2010 through time series Landsat images and phenology-based algorithms. *Remote Sens. Environ.* **2015**, *160*, 99–113. [[CrossRef](#)]
49. Zou, Z.; Dong, J.; Menarguez, M.A.; Xiao, X.; Qin, Y.; Doughty, R.B.; Hooker, K.V.; David Hambright, K. Continued decrease of open surface water body area in Oklahoma during 1984–2015. *Sci. Total Environ.* **2017**, *595*, 451–460. [[CrossRef](#)]
50. Zhao, G.; Li, Y.; Zhou, L.; Gao, H. Evaporative water loss of 1.42 million global lakes. *Nat. Commun.* **2022**, *13*, 3686. [[PubMed](#)]
51. Sen, K.P. Estimates of the Regression Coefficient Based on Kendall's Tau. *Publ. Am. Stat. Assoc.* **1968**, *63*, 1379–1389. [[CrossRef](#)]
52. Mann, H.B. Nonparametric test against trend. *Econometrica* **1945**, *13*, 245–259. [[CrossRef](#)]
53. Kendall, S.B. Enhancement of conditioned reinforcement by uncertainty. *J. Exp. Anal. Behav.* **1975**, *24*, 311–314.
54. Woolway, R.I.; Kraemer, B.M.; Lenters, J.D.; Merchant, C.J.; O'Reilly, C.M.; Sharma, S. Global lake responses to climate change. *Nat. Rev. Earth Environ.* **2020**, *1*, 388–403.
55. Shugar, D.H.; Burr, A.; Haritashya, U.K.; Kargel, J.S.; Watson, C.S.; Kennedy, M.C.; Bevington, A.R.; Betts, R.A.; Harrison, S.; Strattman, K. Rapid worldwide growth of glacial lakes since 1990. *Nat. Clim. Change* **2020**, *10*, 939–945. [[CrossRef](#)]
56. van Dijk, A.; Beck, H.E.; Crosbie, R.S.; de Jeu, R.A.M.; Liu, Y.Y.; Podger, G.M.; Timbal, B.; Viney, N.R. The Millennium Drought in southeast Australia (2001–2009): Natural and human causes and implications for water resources, ecosystems, economy, and society. *Water Resour. Res.* **2013**, *49*, 1040–1057. [[CrossRef](#)]
57. Pi, X.; Luo, Q.; Feng, L.; Xu, Y.; Tang, J.; Liang, X.; Ma, E.; Cheng, R.; Fensholt, R.; Brandt, M.; et al. Mapping global lake dynamics reveals the emerging roles of small lakes. *Nat. Commun.* **2022**, *13*, 5777. [[CrossRef](#)] [[PubMed](#)]
58. Zhu, Y.; Ye, A.; Zhang, Y. Changes of total and artificial water bodies in inland China over the past three decades. *J. Hydrol.* **2022**, *613*, 128344.
59. Liu, Y.; Wu, G.; Zhao, X. Recent declines in China's largest freshwater lake: Trend or regime shift? *Environ. Res. Lett.* **2013**, *8*, 014010. [[CrossRef](#)]
60. Deng, Y.; Jiang, W.; Tang, Z.; Ling, Z.; Wu, Z. Long-term changes of open-surface water bodies in the Yangtze River basin based on the Google Earth Engine cloud platform. *Remote Sens.* **2019**, *11*, 2213.
61. Luo, D.; Jin, H.; Du, H.; Li, C.; Ma, Q.; Duan, S.; Li, G. Variation of alpine lakes from 1986 to 2019 in the Headwater Area of the Yellow River, Tibetan Plateau using Google Earth Engine. *Adv. Clim. Chang. Res.* **2020**, *11*, 11–21. [[CrossRef](#)]

62. Wang, D.; Alimohammadi, N. Responses of annual runoff, evaporation, and storage change to climate variability at the watershed scale. *Water Resour. Res.* **2012**, *48*, W05546.
63. Vorosmarty, C.J.; Green, P.; Salisbury, J.; Lammers, R.B. Global Water Resources: Vulnerability from Climate Change and Population Growth. *Science* **2000**, *289*, 284–288.
64. Biemans, H.; Haddeland, I.; Kabat, P.; Ludwig, F.; Hutjes, R.W.A.; Heinke, J.; von Bloh, W.; Gerten, D. Impact of reservoirs on river discharge and irrigation water supply during the 20th century. *Water Resour. Res.* **2011**, *47*, W03509. [[CrossRef](#)]
65. Zhou, Y.; Dong, J.; Xiao, X.; Xiao, T.; Yang, Z.; Zhao, G.; Zou, Z.; Qin, Y. Open surface water mapping algorithms: A comparison of water-related spectral indices and sensors. *Water* **2017**, *9*, 256.
66. Wang, X.; Wang, W.; Jiang, W.; Jia, K.; Rao, P.; Lv, J. Analysis of the Dynamic Changes of the Baiyangdian Lake Surface Based on a Complex Water Extraction Method. *Water* **2018**, *10*, 1616. [[CrossRef](#)]
67. Fisher, A.; Flood, N.; Danaher, T. Comparing Landsat water index methods for automated water classification in eastern Australia. *Remote Sens. Environ.* **2016**, *175*, 167–182. [[CrossRef](#)]

Disclaimer/Publisher’s Note: The statements, opinions and data contained in all publications are solely those of the individual author(s) and contributor(s) and not of MDPI and/or the editor(s). MDPI and/or the editor(s) disclaim responsibility for any injury to people or property resulting from any ideas, methods, instructions or products referred to in the content.